# Analytical and experimental study of the dynamics of a micro-electromechanical resonator based digital-to-analog converter

OPEN ACCESS
IOP Publishing
Journal of Micromechanics and Microengineering
J. Micromech. Microeng. **31** (2021) 125010 (14pp)
https://doi.org/10.1088/1361-6439/ac3219

# Analytical and experimental study of the dynamics of a micro-electromechanical resonator based digital-to-analog converter

**Wen Zhao**[1], **Sally Ahmed**[2], **Hossein Fariborzi**[2] **and Mohammad I Younis**[1,*]

[1] Physical Sciences and Engineering Division, King Abdullah University of Science and Technology, Thuwal, Saudi Arabia
[2] Computer, Electrical and Mathematical Sciences and Engineering Division, King Abdullah University of Science and Technology, Thuwal, Saudi Arabia

E-mail: Mohammad.Younis@kaust.edu.sa

Received 9 July 2021, revised 26 September 2021
Accepted for publication 21 October 2021
Published 3 November 2021

**Abstract**

In this paper, an analytical model of a micro-electromechanical (MEM) resonator used as a 4-bit digital-to-analog converter (DAC) is presented. First, we derive the dynamic equation of the 4-bit DAC device, and the nonlinear governing equation is solved by the Galerkin method combined with a shooting technique to simulate the static response, linear eigenvalue problem, and forced vibration response of the device for various electrostatic actuation cases. Also, we optimize the air gaps in the linear domain to ensure enhanced performance of the DAC. Further, to analyze the operation of the DAC in the nonlinear regime, two experimental samples powered by −2 dBm and −12 dBm AC inputs are examined. Forward and backward frequency sweeps are conducted experimentally and analytically. The proposed analytical results are validated by comparison with experimental data. The results indicate that the presented modeling, simulations, and optimization are effective tools for the design of MEM resonator-based circuits.

Keywords: digital to analog converter (DAC), MEMS resonator, optimization, nonlinear dynamics

(Some figures may appear in colour only in the online journal)

## 1. Introduction

Micro-beams are the most commonly used structures in micro-electromechanical systems (MEMS) resonators [1, 2]. In particular, clamped-clamped beams, a key resonator component, have been extensively explored for many practical applications such as in band-pass filters [3–5], oscillators, digital logic gates [6–11], and memory devices [12, 13]. The static and dynamic behaviors of resonant beams are complicated, especially under the nonlinear electrostatic-force actuation. Thus, it is necessary to understand the behavior of resonant beams in such cases.

Considerable effort has been made to understand the complex static and dynamic behaviors of MEMS structures, especially beams. A review of recent advances in this field is presented in [14]. Mestrom *et al* [15] studied the softening and hardening behaviors of a clamped-clamped beam resonator through a combined analytical-numerical and experimental approach. The obtained results show softening or hardening nonlinear dynamics depending on excitations. Mestrom *et al* [16] also utilized the clamped-clamped beam resonator

* Author to whom any correspondence should be addressed.

to predict the measured resonator response and the nonlinear dynamic steady-state behaviors under different parameters. A good quantitative match was achieved between simulation and experimental results. Venstra *et al* [17] studied the clamped-clamped mechanical resonators in water through a magnetomotive drive. The results demonstrate that the magnetomotive technique can be used to drive and detect micromechanical resonator vibrations. Azizi *et al* [18] investigated the nonlinear chaotic dynamics of an electrostatically and piezo-electrically actuated clamped-clamped micro beam. The results indicate that an appropriate DC source to piezoelectric layer can passively control the chaotic response of the micro system. Hu *et al* [19] investigated the snap-through, pull-in behaviors and dynamics of an initially curved micro clamped-clamped beam under an electro-dynamical actuation. Kumar *et al* [20] studied the nonlinear dynamics and the internal resonances of a clamped-clamped beam MEMS resonator by using Galerkin based reduced-order model and a finite element method. Their results can serve as guidelines for developing controllers that regulate the displacement of driven mode by its interaction with the coupled mode. Ghayesh *et al* [21] analytically presented an investigation on an electrically actuated MEMS clamped-clamped resonator and studied the pull-in instability, force-response, and dynamic behavior of the system through the time histories and phase-plane portraits. Li *et al* [22] studied the nonlinear modal interactions of electrically actuated clamped-clamped micro beams and the effects of antisymmetric modes on the nonlinear dynamics. The results show that the nonlinear modal interactions can transfer the energy from one mode to a nearby mode.

As mentioned above, the Galerkin method has been widely used to investigate the dynamics of MEMS structures. However, under low damping conditions and for complex electrostatic actuation, the Galerkin method suffers since it can only catch part of the dynamic state (solution). Furthermore, simulations using this method are time-consuming and do not converge easily. To alleviate this, a combined Galerkin-shooting technique can be used [1]. Most resonance curves, especially near the bifurcation point [1, 23], can be captured by this powerful method. Nayfeh *et al* [24] and Younis *et al* [25] adopted a shooting method along with the Galerkin method to study the nonlinear dynamics of a novel MEMS switch excited around the primary resonance and undergoing large motion. Yu *et al* [26] adopted the combined Galerkin-shooting technique to analyze the electromechanical post-buckling response of a clamped-clamped beam actuator subjected to axial residual stresses and a symmetric electrostatic field. Using same technique, Emam *et al* [27] experimentally and analytically investigated the nonlinear behaviors of a clamped-clamped buckled beam near subharmonic resonance and investigate the stability and bifurcations based on a combined method of Galerkin-shooting. Nayfeh and Younis [28] utilized the combination of the shooting technique and a reduced-order model to analyze and simulate the dynamics of an electrically actuated micro-beam, near primary, sub-harmonic, and super-harmonic resonances.

Digital-to-analog converters (DACs) are basic elements for electronics and microcontrollers in MEMS. Recent, efforts have been made to realize DACs using MEMS technology motivated by the need to reduce power consumption, which has a more promising digital signal processing application in MEMS devices [29]. Yeh *et al* [30] demonstrated a technique to create a 3-bit mechanical DAC by using lever arms and thermal actuator arrays. It can take digital electrical signals and produce mechanical displacements at the output which can be used in applications such as micro-optics, mechanical-computing, and micro-robotics. Toshiyoshi *et al* [31] discussed the design and implementation of a 4 bit micromachined electrostatic actuator-based MEMS DAC in which a set of local digital displacements are converted into an analog output displacement. Pandiyan *et al* [32] used a bending beam electro thermal compliant actuator to design and simulate an MEMS-based DAC. The proposed DAC generates a mechanical displacement at the output from the digital input based on the principle of weighted stiffness which is analogous to binary-weighted resistor DAC.

The investigated DACs above based on different microstructures are complicated consisting of arrays of many asymmetric and symmetric structures with multi-bent beam actuators. As a result, these kinds of reported DACs structures occupy large areas. Also, some of the reported DACs need DC currents for their operation, which results in high energy consumption. The proposed DAC here consists of a single straight micro clamped-clamed beam with multi-partial electrodes, which is simple and easy to fabricate. Also, this DAC does not need a DC current, hence it consumes less power. The proposed DAC can be used to internet of things (IoT) applications that demand moderate speed and lower power consumption.

In this paper, we analytically and experimentally investigate the statics and dynamics of the MEMS resonator-based 4-bit DAC [33, 34] in depth. The device consists of a clamped-clamped beam, separated from various partial electrodes of different air-gap sizes. The digital inputs are DC voltages, applied to four partial electrodes, which tune the beam's resonance frequency using the electrostatic softening effect. Our objective is to develop a theoretical model, predict all the relevant aspects of the experimental response, and optimize the device performance. First, we derive the dynamic equations of the device, and then we investigate the static deflection, eigenvalue problem (EVP), optimization, and dynamic response of the micro-resonator based on the Galerkin-shooting procedure. Lastly, we examine two measurement samples of the DAC under the nonlinear operation. The forward and backward frequency sweep on each digital case is conducted, and excellent agreements are found between the experimental and theoretical results.

The outline of the rest of the paper is as follows. Section 2 describes the modeling procedure. The static response, EVP, and optimization are presented in sections 3 and 4, respectively. Section 5 experimentally and analytically illustrates the frequency response for the forward and backward frequency sweeps and examines the effects of the biasing voltage of the beam on the DAC. Finally, conclusions remarks are summarized in the last section.

## 2. Problem formulation

A picture of the proposed resonator DAC is shown in figure 1(a). The device is fabricated by MEMSCAP Inc foundry through SOIMUMPs process [35] using a surface micromachining process on a silicon on an insulator wafer. The process starts by defining electrodes with gold by lifting off a Cr/Au bi-layer (20 nm/500 nm), and then the silicon device layer (25 $\mu$m thick) is patterned by deep reactive ion etching to define the beam, the anchors, and corner electrodes. Finally, the structure is released by etching the $SiO_2$ in using vapor Hydrogen Fluoride (HF) . The used wafer has the following layer thicknesses: (a) silicon thickness: 25 $\pm$ 1 $\mu$m; (b) oxide thickness: 1 $\pm$ 0.05 $\mu$m; (c) handle wafer (substrate) thickness: 400 $\pm$ 5 $\mu$m.

The DAC device consists of an in-plane-clamped-clamped micro beam based resonator (length $l = 500$ $\mu$m, lateral width $W = 2.66$ $\mu$m, thickness $h = 25$ $\mu$m) with a DC voltage ($V_{\text{Beam}}$), and side partial electrodes with various air-gap widths as shown in figure 1(b). The digital inputs of the DAC are DC voltages, applied to four corner electrodes marked as $D_3$, $D_2$, $D_1$, and $D_0$ in figure 1(a). The actuation of the micro beam resonator is realized through the different digital input combinations (DC source) and AC voltage components. The resonator here is driven to vibrate on the first vibration mode.

The input vector $D_3$ $D_2$ $D_1$ $D_0$ is a binary number where $D_3$ (with the smallest gap) is the most significant bit and $D_0$ (with the largest gap) is the least significant bit. Each bit can be either '1' (on) or '0' (off), which are defined as '40' V or '0' V, respectively. Thus, there are 16 combinations ($2^4 = 16$) for the inputs ranging from '0000' to '1111' representing the decimal numbers from 0 to 15. The resonance frequency of the beam should increase as the decimal equivalent value of the applied digital input increases.

The equations of motion governing the transverse deflection $\hat{w}$ of a clamped-clamped beam under the partial electrode actuation can be described as

$$\begin{aligned}
&EI\,\hat{w}'''' + \rho A\,\ddot{\hat{w}} + \hat{c}\,\dot{\hat{w}} \\
&\quad = \left[\hat{N} + \frac{EA}{2l}\int_0^l (\hat{w}(\hat{x},\hat{t})')^2 \mathrm{d}\hat{x}\right]\hat{w}'' \\
&\qquad + \left[\frac{1}{2}\varepsilon b\frac{(V_{\text{D1}} - V_{\text{Beam}})^2}{(d_1 - \hat{w})^2} - \frac{1}{2}\varepsilon b\frac{(V_{\text{D0}} - V_{\text{Beam}})^2}{(d_0 + \hat{w})^2}\right] \\
&\qquad [U(\hat{a}_5 - \hat{x}) - U(\hat{a}_4 - \hat{x})] \\
&\qquad + \left[\frac{1}{2}\varepsilon b\frac{(V_{\text{Beam}} - V_{\text{AC}}\cos(\Omega\hat{t}))^2}{(d - \hat{w})^2} - \frac{1}{2}\varepsilon b\frac{{V_{\text{Beam}}}^2}{(d + \hat{w})^2}\right] \\
&\qquad [U(\hat{a}_3 - \hat{x}) - U(\hat{a}_2 - \hat{x})] \\
&\qquad + \left[\frac{1}{2}\varepsilon b\frac{(V_{\text{D3}} - V_{\text{Beam}})^2}{(d_3 - \hat{w})^2} - \frac{1}{2}\varepsilon b\frac{(V_{\text{D2}} - V_{\text{Beam}})^2}{(d_2 + \hat{w})^2}\right] \\
&\qquad [U(\hat{a}_1 - \hat{x}) - U(\hat{a}_0 - \hat{x})]] \qquad (1)
\end{aligned}$$

with the following boundary conditions:

$$\hat{w}(0,\hat{t}) = \hat{w}(l,\hat{t}) = 0 \text{ and } \hat{w}'(0,\hat{t}) = \hat{w}'(l,\hat{t}) = 0 \qquad (2)$$

where the prime indicates the derivative in space $\hat{w}'(\hat{x},\hat{t}) = \frac{\partial \hat{w}}{\partial \hat{x}}$ and the dot indicates the derivative in time $\dot{\hat{w}}(\hat{x},\hat{t}) = \frac{\partial \hat{w}}{\partial \hat{t}}$.

Here, $x$ is the position along the beam length, $E$ and $I$ are the elastic modulus and the moment of inertia, $b$ is the width of the beam, $h$ is the beam thickness, $\hat{c}$ is the viscous damping coefficient, $\hat{N}$ is the axial load, $A$ is the cross-section area of the beam, $l$ is the length of the beam, $d$ is the gap between the beam and drive or sense electrode. The air gaps between the corner electrodes and beam are $d_0$, $d_1$, $d_2$, and $d_3$, respectively. Also, $U(x)$ is a step function. The distance of each partial electrode position to the left starting point ($o$) of the resonator in figure 1(a) is $\hat{a}_i$ ($i = 0, 1, 2, 3, 4, 5$) respectively. The detailed values are illustrated in table 1.

Equation (1) is governed by 16 key parameters ($d_1$, $d_2$, $d_3$, $d_4$, $d$, and $\hat{a}_0, \hat{a}_1, \hat{a}_2, \hat{a}_3, \hat{a}_4, \hat{a}_5$, $V_{\text{D0}}$, $V_{\text{D1}}$, $V_{\text{D2}}$, $V_{\text{D3}}$, $V_{\text{Beam}}$). To facilitate analysis of the equation, the following dimensionless variables are introduced

$$w = \frac{\hat{w}}{d_3}; \quad x = \frac{\hat{x}}{l}; \quad t = \hat{t}\sqrt{\frac{\rho b h l^4}{EI}}; \quad a_i = \frac{\hat{a}_i}{l}. \qquad (3)$$

We substitute equation (3) into equations (1) and (2), yielding the non-dimensional equation

$$\begin{aligned}
&w'''' + \ddot{w} + c\,\dot{w} \\
&\quad = \left[N_{\text{non}} + \alpha_1\int_0^1 (w(x,t)')^2 \mathrm{d}x\right] w'' \\
&\qquad + \alpha_2\left[\frac{(V_{\text{D1}} - V_{\text{Beam}})^2}{(\frac{d_1}{d_3} - w)^2} - \frac{(V_{\text{D0}} - V_{\text{Beam}})^2}{(\frac{d_0}{d_3} + w)^2}\right] \\
&\qquad [U(a_5 - x) - U(a_4 - x)] \\
&\qquad + \alpha_2\left[\frac{(V_{\text{Beam}} - V_{\text{AC}}\cos(\Omega t))^2}{(\frac{d}{d_3} - w)^2} - \frac{{V_{\text{Beam}}}^2}{(\frac{d}{d_3} + w)^2}\right] \\
&\qquad [U(a_3 - x) - U(a_2 - x)] \\
&\qquad + \alpha_2\left[\frac{(V_{\text{D3}} - V_{\text{Beam}})^2}{(1 - w)^2} - \frac{(V_{\text{D2}} - V_{\text{Beam}})^2}{(\frac{d_2}{d_3} + w)^2}\right] \\
&\qquad [U(a_1 - x) - U(a_0 - x)]]. \qquad (4)
\end{aligned}$$

The above is subjected to the non-dimensional boundary conditions:

$$w(0,t) = w(1,t) = 0; \quad w'(0,t) = w'(1,t) = 0. \qquad (5)$$

The non-dimensional parameters appearing in equation (4) are

$$\alpha_1 = 6\left(\frac{d_3}{b}\right)^2; \alpha_2 = \frac{6\varepsilon l^4}{Eb^3{d_3}^3}; N_{\text{non}} = \frac{l^2}{EI}\hat{N}. \qquad (6)$$

The deflection of the clamped-clamped micro beam under the electrostatic force is expressed as a static normalized

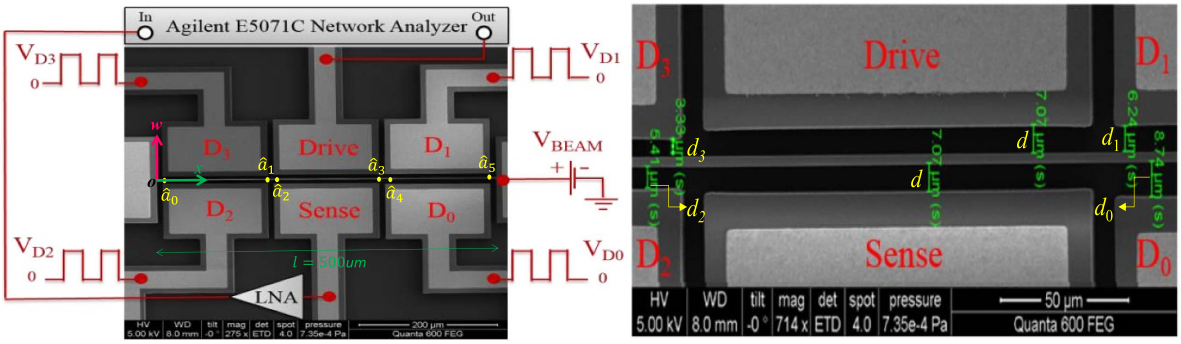


(*a*) (*b*)

**Figure 1.** (a) Experimental setup with an SEM image of the fabricated micro-resonator DAC; (b) A zoomed-in picture showing the dimensions of the obtained air gaps after fabrication. © 2020 IEEE. Reprinted, with permission, from [34].

**Table 1.** The specifications of the resonator.

| Symbol | Value | Quantity | Value |
|---|---|---|---|
| $d_0$ | 8.74 $\mu$m | $\hat{a}_0$ | 8 $\mu$m |
| $d_1$ | 6.24 $\mu$m | $\hat{a}_1$ | 163.9 $\mu$m |
| $d_2$ | 5.41 $\mu$m | $\hat{a}_2$ | 171.9 $\mu$m |
| $d_3$ | 3.33 $\mu$m | $\hat{a}_3$ | 327.8 $\mu$m |
| $d$ | 7.075 $\mu$m | $\hat{a}_4$ | 335.8 $\mu$m |
| $l$ | 500 $\mu$m | $\hat{a}_5$ | 491.7 $\mu$m |
| $h$ | 25 $\mu$m | $W$ | 2.66 $\mu$m |

deflection $w_s(x)$ due to the DC voltage component and a normalized dynamic component due to the AC source, denoted by $w_d(x, t)$; that is

$$w(x,t) = w_s(x) + w_d(x,t). \tag{7}$$

To determine $w_s(x)$, we set the time derivative and the AC forcing terms in equation (4) equal zero and obtain

$$\begin{aligned} w_s(x)'''' - \left[N_{non} + \alpha_1 \int_0^1 (w_s(x)')^2 dx\right] w_s(x)'' \\ = +\alpha_2 \left[\frac{(V_{D1} - V_{Beam})^2}{(\frac{d_1}{d_3} - w_s)^2} - \frac{(V_{D0} - V_{Beam})^2}{(\frac{d_0}{d_3} + w_s)^2}\right] \\ [U(a_5 - x) - U(a_4 - x)] \\ + \alpha_2 \left[\frac{V_{Beam}{}^2}{(\frac{d}{d_3} - w_s)^2} - \frac{V_{Beam}{}^2}{(\frac{d}{d_3} + w_s)^2}\right] \\ [U(a_3 - x) - U(a_2 - x)] \\ + \alpha_2 \left[\frac{(V_{D3} - V_{Beam})^2}{(1 - w_s)^2} - \frac{(V_{D2} - V_{Beam})^2}{(\frac{d_2}{d_3} + w_s)^2}\right] \\ [U(a_1 - x) - U(a_0 - x)]] \end{aligned} \tag{8}$$

with the associated boundary conditions

$$w_s(0,t) = w_s(1,t) = 0; w_s'(0,t) = w_s'(1,t) = 0. \tag{9}$$

By plugging equation (7) into equation (4), and only keeping linear terms of $w_d$ after the electrostatic force is expanded in $w_d$ by Taylor series expansions, we obtain

$$\begin{aligned} w_d(x,t)'''' + w_s(x,t)'''' + \ddot{w}_d(x,t) + c\dot{w}_d(x,t) \\ = \left[N_{non} + \alpha_1 \int_0^l (w_d(x,t)' + w_s(x,t)')^2 dx\right] \\ (w_d(x,t)'' + w_s(x,t)'') \\ + \alpha_2 \left[(V_{D1} - V_{Beam})^2 \left[\frac{1}{(\frac{d_1}{d_3} - w_s)^2} + \frac{2w_d}{(\frac{d_1}{d_3} - w_s)^3}\right]\right. \\ \left. -(V_{D0} - V_{Beam})^2 \left[\frac{1}{(\frac{d_0}{d_3} + w_s)^2} - \frac{2w_d}{(\frac{d_0}{d_3} + w_s)^3}\right]\right] \\ [U(a_5 - x) - U(a_4 - x)] \\ + \alpha_2 \left[(V_{Beam} + V_{AC}\cos(\Omega t))^2 \left[\frac{1}{(\frac{d}{d_3} - w_s)^2} + \frac{2w_d}{(\frac{d}{d_3} - w_s)^3}\right]\right. \\ \left. -V_{Beam}{}^2 \left[\frac{1}{(\frac{d}{d_3} + w_s)^2} - \frac{2w_d}{(\frac{d}{d_3} + w_s)^3}\right]\right] \\ [U(a_3 - x) - U(a_2 - x)] \\ + \alpha_2 \left[(V_{D3} - V_{Beam})^2 \left[\frac{1}{(1 - w_s)^2} + \frac{2w_d}{(1 - w_s)^3}\right]\right. \\ \left. -(V_{D2} - V_{Beam})^2 \left[\frac{1}{(\frac{d_2}{d_3} + w_s)^2} - \frac{2w_d}{(\frac{d_2}{d_3} + w_s)^3}\right]\right] \\ [U(a_1 - x) - U(a_0 - x)]]. \end{aligned} \tag{10}$$

By eliminating the terms representing the equilibrium position of equation (8) and the AC term from equation (10), this yields:

$$
\begin{aligned}
&w_{\mathrm{d}}(x,t)'''' + \ddot{w}_{\mathrm{d}}(x,t) + c\dot{w}_{\mathrm{d}}(x,t) \\
&\quad = [N_{\mathrm{non}} + \alpha_1 \int_0^l (w_{\mathrm{s}}(x)')^2 \mathrm{d}x] w_{\mathrm{d}}(x,t)'' \\
&\qquad + \alpha_1 \left[ \int_0^l ((w_{\mathrm{d}}(x,t)')^2 + 2w_{\mathrm{d}}(x,t)'w_{\mathrm{s}}(x)')\mathrm{d}x \right] \\
&\qquad [w_{\mathrm{d}}(x,t)'' + w_{\mathrm{s}}(x)''] \\
&\qquad + \alpha_2 \left[ \frac{2(V_{\mathrm{D1}} - V_{\mathrm{Beam}})^2}{(\frac{d_1}{d_3} - w_{\mathrm{s}})^3} \right] + \frac{2(V_{\mathrm{D0}} - V_{\mathrm{Beam}})^2}{(\frac{d_0}{d_3} + w_{\mathrm{s}})^3} ] w_{\mathrm{d}} \\
&\qquad [U(a_5 - x) - U(a_4 - x)] \\
&\qquad + \alpha_2 \left[ \frac{2V_{\mathrm{Beam}}^2}{(\frac{d}{d_3} - w_{\mathrm{s}})^3} + \frac{2{V_{\mathrm{Beam}}}^2}{(\frac{d}{d_3} + w_{\mathrm{s}})^3} \right] w_{\mathrm{d}} \\
&\qquad [U(a_3 - x) - U(a_2 - x)] \\
&\qquad + \alpha_2 \left[ \frac{2(V_{\mathrm{D3}} - V_{\mathrm{Beam}})^2}{(1 - w_{\mathrm{s}})^3} + \frac{2(V_{\mathrm{D2}} - V_{\mathrm{Beam}})^2}{(\frac{d_2}{d_3} + w_{\mathrm{s}})^3} \right] w_{\mathrm{d}} \\
&\qquad [U(a_1 - x) - U(a_0 - x)]]
\end{aligned}
\tag{11}
$$

with the associated boundary condition

$$
w_{\mathrm{d}}(0,t) = w_{\mathrm{d}}(1,t) = 0; {w_{\mathrm{d}}}'(0,t) = {w_{\mathrm{d}}}'(1,t) = 0. \tag{12}
$$

In the following analysis, we only consider the 3-bit DAC while keeping the $D_0$ un-actuated to compare the analytical result with the experimental data reported in [33, 34]. The air gaps between the beam and the corner electrodes are adjusted based on the weight of each bit such that the more significant bits have stronger effects on the beam. This is realized by making the gap of $D_0$ the largest while making the gap of $D_3$ the smallest.

Next, we resort to the Galerkin procedure [1] to solve for the EVP and dynamic responses of the system by assuming the micro-beam deflection as

$$
w(x,t) = \sum_{i=1}^{N} u_i(t)\phi_i(x) \tag{13}
$$

where $\varphi_i(x)$ is the $i$th mode shape of the micro-beam at zero voltage load and $u_j$ is its modal amplitude. Equation (13) is then substituted into equation (11) for the EVP, and equation (4) for the forced vibration response, then we multiply the outcome by the mode shape, apply the orthogonality condition of the mode shapes, and integrate over the beam domain from 0 to l. A convergence study needs to be conducted to determine the minimum number of modes that are needed to capture the dynamic behavior accurately [1]. In this work, for simplicity, we use a single-mode to approximate the dynamic response. The obtained analytical results reach good agreement with the experimental ones. Thus, a single-mode yields sufficient accuracy.

## 3. Static deflection analysis

Here, we examine the static response to better understand how static deflection can impact the system behavior. We explore and simulate the static response for each digital combination cases. For the static analysis, due to the complicated denominator of forcing terms in equation (8), the solution does not easily converge and the adoption of the Galerkin method is time-consuming. To improve the efficiency of simulations, and obtain more accurate results, we resort to a shooting method to solve such equations [36, 37].

Next, we solve the static response based on the shooting method with the boundary value problem. We shoot for the value of the complicated integral mid-plane stretching term of equation (8) iteratively by the Newton Raphson method until achieving convergence to within a very small predefined tolerance. Figure 2 shows the static deflections along the micro beam for eight different digital input combination cases from case-000 to case-111.

From figure 2, the static deflection curve and the maximum deflection point of the micro beam for different digital input combinations are illustrated. We conclude that the static deflection curves vary for different digital input combinations. Also, we observe that the multi-actuated electrode configuration for the digital input can shift the maximum deflection along the micro beam. This is due to the fact that the generated electrostatic force by different digital combinations varies along the beam, and also due to the digital electrodes with different gap widths. Therefore, the maximum position along the micro beam varies with the digital input combinations.

For example, the digital case-010 (the bits D3 and D1 are off while the D2 is on) exhibits the maximum static deflection. The electrode D3 with the smallest air-gap generates the largest electrostatic force, and then the partial electrodes D3 and D1 on the same side of the beam work together to yield the higher amplitude response. However, for the digital case-111, the electrostatic force generated by the connected corner partial electrodes (D3 D2 D1) neutralize the ones from the micro beam, thus, almost zero amplitude is generated in this case. To examine case-100, one can see that D3 is digitally connected while the D2 and D1 are not connected, which means the electrostatic force generated by electrodes D2 and D3 works on the beam. But these forces mainly concentrate on the area around the anchor of either side of the micro beam, which bends the micro beam. Thus, the static deflection for case-100 is similar to a sinusoidal function.

We notice that, compared to the smallest air gaps ($d_3 = 3.33$ $\mu$m), the maximum deflection for every single digital case is very weak, particularly for the digital case-111. Thus, in other words, the static deflection of the micro beam at 40 V is almost zero which is negligible. As a result, we will neglect the static deflection $w_{\mathrm{s}}$ $(x)$ when solving the EVP in the following section.

## 4. Linear EVP

As pointed out previously, the static deflection is very low when digital partial electrodes 40 V are connected. Hence, to

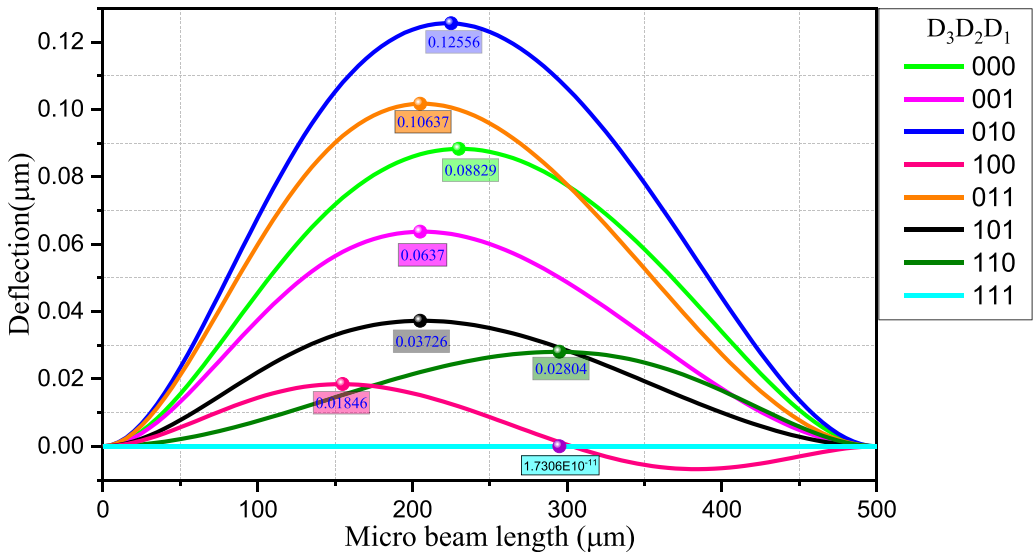


**Figure 2.** The static deflection curves and marked maximum deflection point of the beam for different digital input combinations.

ease the computational cost, we solve the EVP in equations (11) and (12) without the damping term, while also neglecting the static deflection $w_s(x)$. We apply a single-mode in the Galerkin model, and convert the partial differential equation into an ordinary differential equation. Then, we collect the coefficients of the linear term $u(t)$; and take its square root, which yields the following expression for the first natural (resonance) frequency of the beam under electrostatic actuation:

$$\text{Freq (kHz)} = \frac{\sqrt{-0.00684568\left[\frac{(V_{D0}-V_{Beam})^2 d_3{}^3}{d_0{}^3}+\frac{(V_{D1}-V_{Beam})^2 d_3{}^3}{d_1{}^3}\right]-0.00679926\left(\frac{(V_{D2}-V_{Beam})^2 d_3{}^3}{d_2{}^3}+(V_{D3}-V_{Beam})^2\right)-\frac{0.072397 V_{Beam}{}^2 d_3{}^3}{d^3}+20.5004^2}}{2\pi T\times 1000}. \quad (14)$$

Note that the resonance frequency of the resonator is a complicated function of eight key parameters. Based on equation (14), the resonance frequency of a resonator can be further analyzed and optimized.

To study the operation of the DAC in the linear domain, we experimentally test the DAC device under a large vacuum level. Figure 3(a) shows the measured frequency curves for different eight input combinations. For the resonator to work as a DAC, the frequency of the drive signal should be fixed at a selected operating frequency, for example, $f_1$ or $f_2$, and the output level should decrease or increase when a digital input is applied. Figure 3(b) shows the time response when the drive frequency is fixed around $f_1$. The resonance frequencies extracted from the experiment, figure 3(a), are plotted in figure 3(c), in which the frequency shifts range from 81.807 kHz for case-000 to 82.670 kHz for case-111. Based on the derived equation (14), the analytical resonance frequencies of the resonator for different input combinations are shown in figure 3(d). One can note good agreement between the analytical and experimental results.

However, it is noticed that the experimentally obtained frequency response curves in figure 3(a) indicate considerable overlaps for the output under different combinations, which makes the amplitude levels created by different inputs at $f_1$ or $f_2$ very close and undistinguishable. Also, the range of the frequency-shifting for different electrode combinations is not large. It is difficult to separate each frequency curve, which is a basic requirement for the proper operation of the DAC [34]. Here, there are two explanations. One is the voltage generated by partial electrodes can partly neutralize the one from the micro beam. The effective power source to trigger the micro resonator, as a result, will be reduced if more partial electrodes are joined. Another one is that the four corner electrodes close to the anchor of the micro beam have less influence on its actuation/deformation.

To overcome this, one can optimize the sizes of air gaps to generate various electrostatic forces along the micro beam under different digital combination cases. By changing air gaps, the distribution of electrostatic force along the micro beam can be reallocated. The expected frequency shift for each case can be improved by optimizing the air gap sizes.

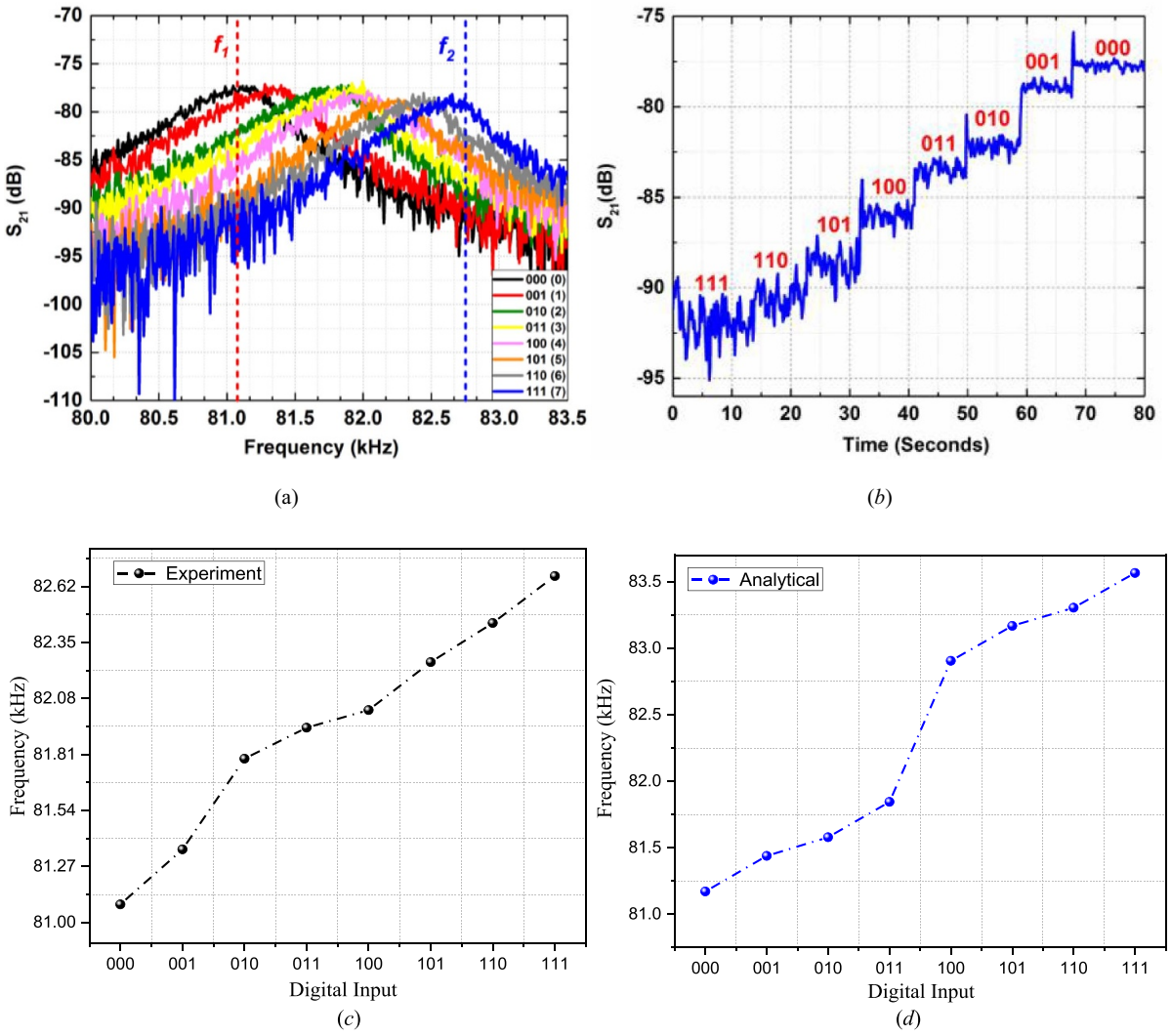


**Figure 3.** The resonance frequency of the beam for 3-bit-DAC (eight different input combinations). (a) Measured resonance peaks of the resonator for each digital input combinations (50 V beam bias, 40 V digital '1', 4.7 Torr, −2 dBm AC drive power. (b) Time-response curve obtained experimentally by fixing the frequency of the drive signal at $f_1$ and varying the applied digital inputs, which shows how the resonator can work as a DAC. © 2020 IEEE. Reprinted, with permission, from [34]. (c) The resonance frequencies of the beam obtained experimentally for different input combinations. (d) Analytical resonance frequencies obtained from the developed model.

$$\text{Freq(kHz)} = \frac{\sqrt{-0.25107\times10^{-18}\left(\frac{(V_{D2}-V_{Beam})^2}{{d_2}^3}+\frac{(V_{D3}-V_{Beam})^2}{{d_3}^3}\right)-0.252784\times10^{-18}\frac{(V_{D1}-V_{Beam})^2}{{d_1}^3}-0.26823\times10^{-18}\frac{{V_{Beam}}^2}{d^3}+20.5004^2}}{2\pi T\times1000}. \quad (15)$$

To optimize the air gaps, we introduce $d_s$ as a basic scaling parameter, valued at $d_s = 5$ $\mu$m, for normalization ($w = \hat{w}/d_s$). This process will enable us to optimize all the gaps including $d_1$, $d_2$, $d_3$, and $d$. It is worthy to note that the new normalization-based $d_s$ here is mainly responsible for the optimization part. Applying the same normalization procedure to the obtained equation (14), Here, we resort to multi-objective goal attainment problems [38] of all the gaps including $d_1$, $d_2$, $d_3$, and $d$. We optimize the gaps over the size range from 2 $\mu$m to 8 $\mu$m. Next, we define a target function and restricted conditions. The restrictions need to satisfy the following conditions: (a) the difference between each neighboring digital frequency is larger than 0.3 kHz in

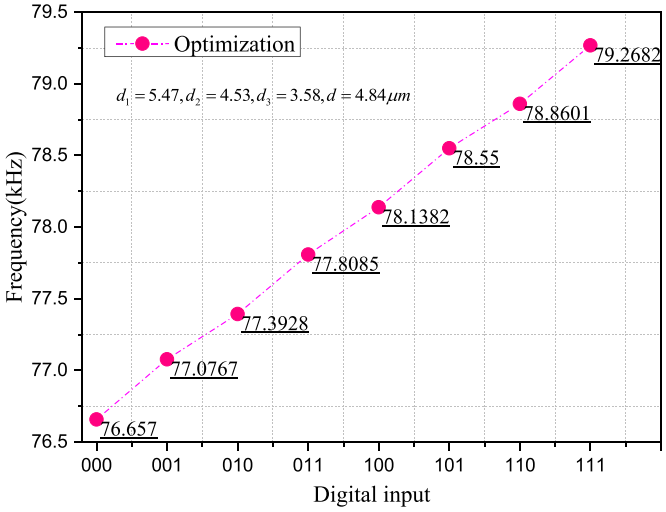


**Figure 4.** The resonance frequency for each digital case after optimization under the following conditions: $V_{\text{Beam}} = 50$ V, digital '1' = 40 V, digital '0' = 40 V.

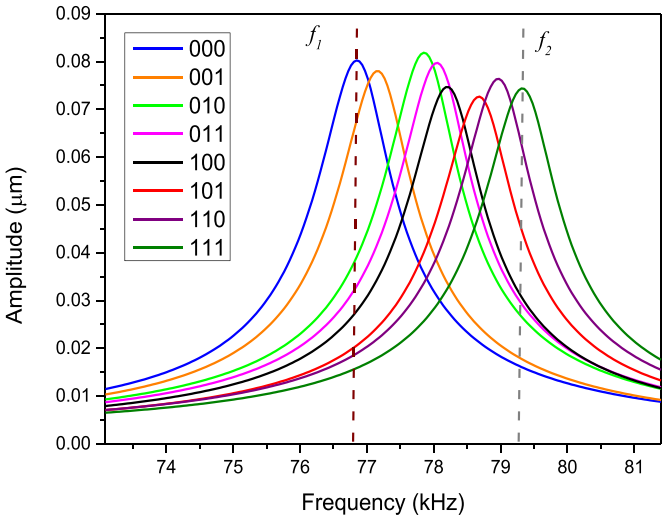


**Figure 5.** Forward frequency sweeps for the resonator working in the linear regime for each input combination under the following conditions: damping $c = 0.25$, $V_{\text{Beam}} = 50$ V, digital '1' = 40 V, digital '0' = 40 V.

a specific domain; (b) the frequency difference between the last case (111) and first case (000) is not too far away; (c) and the frequency linearly and monotonically increase between each case. We optimize the frequency based on the equation (15). The outcome of the optimized gaps is $d_1 = 5.47$ $\mu$m, $d_2 = 4.53$ $\mu$m, $d_3 = 3.58$ $\mu$m, $d = 4.84$ $\mu$m. The simulation results based on these values are shown in figure 4. As noted in figure 4, the resonance frequencies for each digital case are linearly ordered.

## 5. Forced vibration response

To further study the forced vibration response of the microbeam, we apply the procedure of the Galerkin discretization with a single-mode. First, we substitute equation (13) into equation (4), multiply both sides of the outcome by $\varphi_j$, and then we integrate the results from the beam domain zero to one. The outcome yields:

$$\begin{aligned}
&\ddot{u}_1(t) + c\dot{u}_1(t) + \omega_{\text{non}}^2 u_1(t) \\
&= \alpha_1 \int_0^1 (\phi'_1(x)u_1(t))^2 \mathrm{d}x \int_0^1 \phi_1(x)\phi''_1(x)\mathrm{d}x\, u_1(t) \\
&\quad + \alpha_2[(V_{\text{D1}} - V_{\text{Beam}})^2 \int_0^1 \frac{\phi_1(x)}{(\frac{d_1}{d_3} - \phi_1(x)u_1(t))^2} \\
&\quad [U(a_5 - x) - U(a_4 - x)]\mathrm{d}x - (V_{\text{D0}} - V_{\text{Beam}})^2 \\
&\quad \int_0^1 \frac{\phi_1(x)}{(\frac{d_0}{d_3} + \phi_1(x)u_1(t))^2}[U(a_5 - x) - U(a_4 - x)]\mathrm{d}x \\
&\quad + \alpha_2[(V_{\text{Beam}} - V_{\text{ac}}\cos(\Omega\, t))^2 \int_0^1 \frac{\phi_1(x)}{(\frac{d}{d_3} - \phi_1(x)u_1(t))^2} \\
&\quad [U(a_3 - x) - U(a_2 - x)]\mathrm{d}x - V_{\text{Beam}}{}^2 \\
&\quad \int_0^1 \frac{\phi_1(x)}{(\frac{d}{d_3} + \phi_1(x)u_1(t))^2}[U(a_3 - x) - U(a_2 - x)]\mathrm{d}x \\
&\quad + \alpha_2[(V_{\text{D3}} - V_{\text{Beam}})^2 \int_0^1 \frac{\phi_1(x)}{(1 - \phi_1(x)u_1(t))^2} \\
&\quad [U(a_1 - x) - U(a_0 - x)]\mathrm{d}x - (V_{\text{D2}} - V_{\text{Beam}})^2 \\
&\quad \int_0^1 \frac{\phi_1(x)}{(\frac{d_2}{d_3} + \phi_1(x)u_1(t))^2}[U(a_1 - x) - U(a_0 - x)]\mathrm{d}x. \quad (16)
\end{aligned}$$

Next, we rewrite equation (16) by assuming $u_1(t) = Y$ as below

$$\begin{aligned}
&\ddot{Y} + c\dot{Y} + w_{\text{non}}^2 Y \\
&= a_1 \int_0^1 (\phi_1(x)')^2 \mathrm{d}x \int_0^1 \phi_1(x)\phi_1(x)''\, \mathrm{d}x\, Y^3 \\
&\quad + a_2[(V_{\text{D1}} - V_{\text{Beam}})^2 F_1(t) - (V_{\text{D0}} - V_{\text{Beam}})^2 F_2(t)] \\
&\quad + a_2[(V_{\text{Beam}} - V_{\text{AC}}\cos(\Omega t))^2 F_3(t) - V_{\text{Beam}}{}^2 F_4(t)] \\
&\quad + a_2[(V_{\text{D3}} - V_{\text{Beam}})^2 F_5(t) - (V_{\text{D2}} - V_{\text{Beam}})^2 F_6(t)] \quad (17)
\end{aligned}$$

in which $Y$ is a modal coordinate amplitude. Above, the various function $F_i(Y)$ are defined as

$$\begin{aligned}
F_1(Y) &= \int_0^1 \frac{\phi_1(x)}{[\frac{d_1}{d_3} - \phi_1(x)Y]^2}[U(a_5 - x) - U(a_4 - x)]\mathrm{d}x;\ F_2(Y) \\
&= \int_0^1 \frac{\phi_1(x)}{[\frac{d_0}{d_3} + \phi_1(x)Y)]^2}[U(a_5 - x) - U(a_4 - x)]\mathrm{d}x \\
F_3(Y) &= \int_0^1 \frac{\phi_1(x)}{[\frac{d}{d_3} - \phi_1(x)Y]^2}[U(a_3 - x) - U(a_2 - x)]\mathrm{d}x;\ F_4(Y) \\
&= \int_0^1 \frac{\phi_1(x)}{[\frac{d}{d_3} + \phi_1(x)Y]^2}][U(a_3 - x) - U(a_2 - x)]\mathrm{d}x \\
F_5(Y) &= \int_0^1 \frac{\phi_1(x)}{[1 - \phi_1(x)Y]^2}[U(a_1 - x) - U(a_0 - x)]\mathrm{d}x;\ F_6(Y) \\
&= \int_0^1 \frac{\phi_1(x)}{[\frac{d_2}{d_3} + \phi_1(x)Y]^2}][U(a_1 - x) - U(a_0 - x)]\mathrm{d}x. \quad (18)
\end{aligned}$$

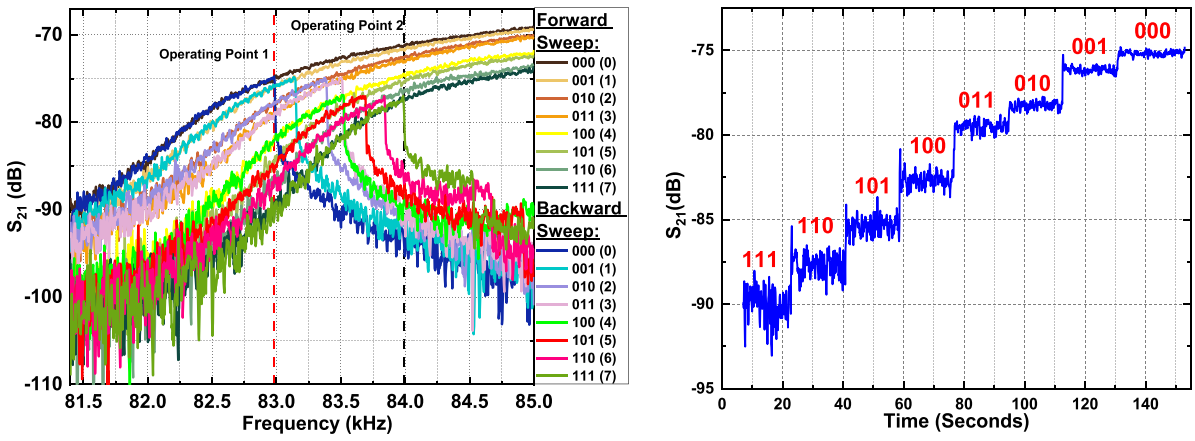


(*a*) (*b*)

**Figure 6.** Experimentally forward and backward frequency sweeps for the resonator working in the non-linear regime for each input combination under the following conditions: 40 mTorr, 40 V beam bias, 40 V digital '1', 0 V digital '0' and −2 dBm input AC signal power in (a) frequency response (b) the $S_{21}$ parameter for transitions from 111 to 000 in descending order at $f_1$. © 2020 IEEE. Reprinted, with permission, from [34].

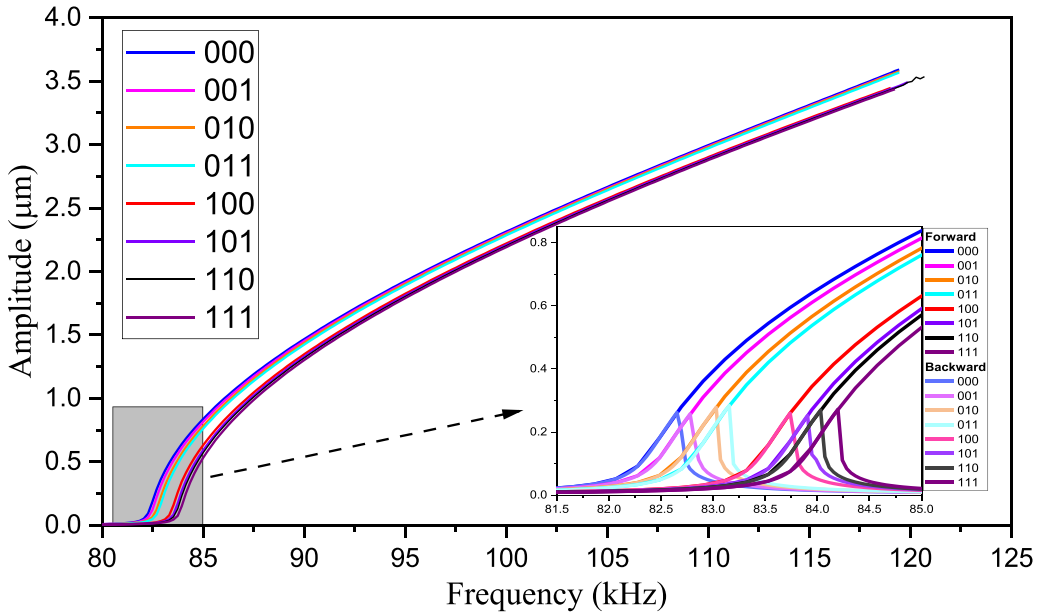


**Figure 7.** Simulated frequency response curves under each digital input combination under the following conditions: $V_{\text{Beam}} = 40$ V, digital '1' = 40 V, digital '0' = 40 V, damping $c = 0.0025$.

Due to the term with $Y$ in the denominator of the electrostatic force terms, the integral terms are not easily evaluated, which will cause computational problems [1, 39]. One approach to resolve this issue is by pre-calculating numerically these complicated terms $F_1(Y), F_2(Y), F_3(Y), F_4(Y), F_5(Y), F_6(Y)$ of equation (18) for each step of $\Delta Y = 0.05$, and then tabulate and store them, as shown in the appendix. Once the table is built, it can be recalled for each time step of the needed numerical integration. Next, we can adopt the shooting technique to solve the forced vibration problem based on equation (17) combined with equation (18). It is noted that the shooting method [1] is a powerful numerical technique that is widely used to capture the periodic motions of the system, including the stable and unstable branches of the solutions. The stability of the periodic solution also can be assessed using the Floquet theory.

Here, to clarify the DAC function well in the linear domain, we solve the forced vibration response by the method of shooting and conduct the frequency sweeps around the primary resonance by using the optimized air gap sizes. One can notice that the frequency for each digital case in figure 5 shows linear response and shift to the higher frequency due to the different digital input ranging from the case-000 to case-111. When the DAC resonator is operated at any single driven frequency signal such as $f_1$ or $f_2$, the corresponding output response can be clearly distinguished. For example, the output level, at different driving signals $f_1$ or $f_2$, can significantly decrease or increase when subjected to the different digital input bits.

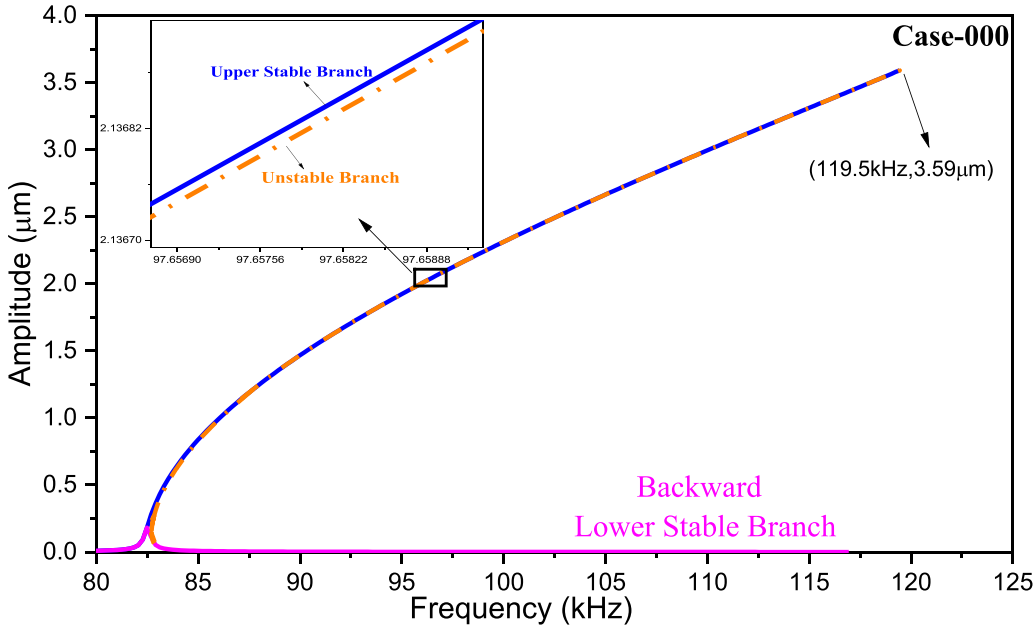


**Figure 8.** The frequency-amplitude response for digital case-000.

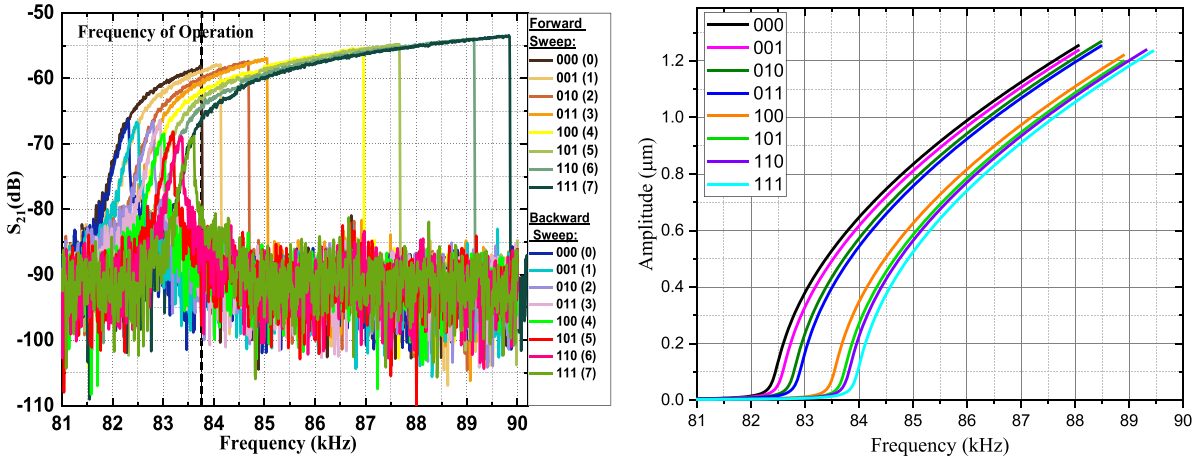


(*a*) (*b*)

**Figure 9.** Forward and backward frequency sweep for the resonator working in the non-linear regime for each input combination under the following conditions: 40 mTorr, 40 V beam bias, 40 V digital '1', 0 V digital '0' and −12 dBm: (a) experimental, (b) simulation. © 2020 IEEE. Reprinted, with permission, from [34].

Therefore, the optimized resonator-based DAC can function well in the linear domain compared to the previously proposed one of figure 3(a).

It is worthy to mention that the proposed resonator-based DAC also can work in the nonlinear regime. Next, we can examine the operation of the proposed DAC in the nonlinear regime if we properly adjust the input power source and vacuum level (damping). Here, two experimental samples with very low damping are considered. It is noted that the frequency response curves are evaluated by calculating the average amplitude response value between maximum and minimum of the steady-state response for each case when conducting time integration.

Here, we compare the experimental data with the analytical results [34]. Figure 6(a) experimentally demonstrates the forward and backward frequency sweep of the resonator in the nonlinear regime for all digital combinations under −2 dBm AC input power level. Due to the different air gap sizes between the beam and digital input electrodes, distributions of the electrostatic load will be non-uniform along the micro beam and it will generate differences for each of the input combinations. In the nonlinear operation, one can notice that the amplitude response in the forward frequency sweep bends to higher values, nonlinear hardening behavior, due to the dominant mid-stretching nonlinearity over the softening electrostatic one. Figure 6(b) shows the $S_{21}$ parameter subjected

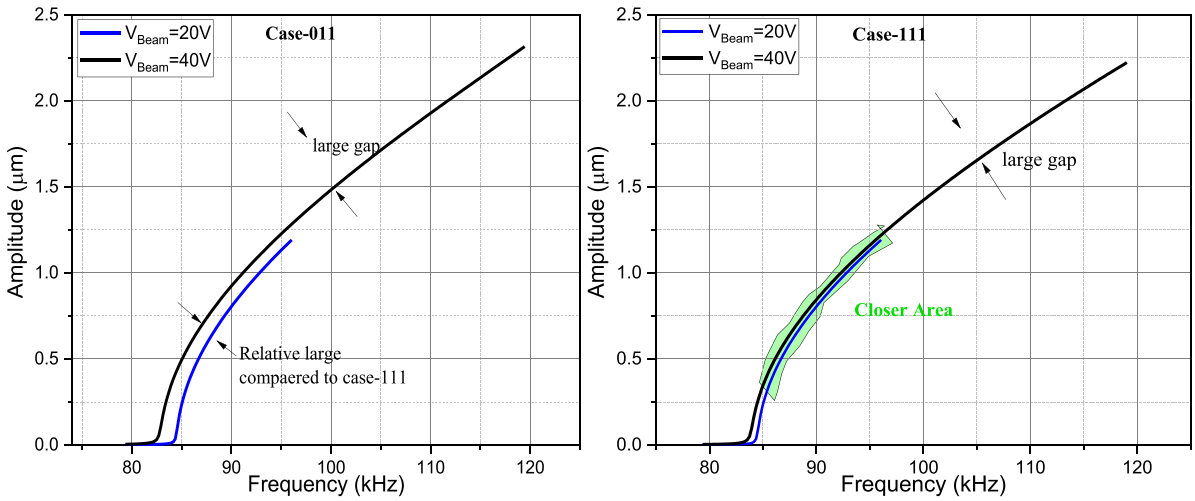


(*a*) (*b*)

**Figure 10.** The effect of $V_{\text{Beam}}$ on the DAC operation of the condition 40 V digital '1', 0 V digital '0', damping $c = 0.0025$ and AC $= -2$ dBm power level (a) for digital case-011; (b) for digital case-111.

to the digital inputs ranging from case-111 to case-000, in descending order. We can see that the digital case-000 input has the largest amplitude at operating point $f_1$ while case-111 has the smallest one. That is because the digital bits for case-111 generates the least influence on the actuation of the micro beam.

The frequencies are swept under different digital input combinations and the inset for forward and backward frequency is shown in figure 7. The analytical results of figure 7 have good agreement with the experiment data of figure 6(a). To better understand the behavior at reached maximum excitation frequency point, we examine their eigenvalues (Floquet Multipliers) at that point. We found that the Multipliers of the system gradually approach the boundary of the unit circle when the excitation increases, and then the microsystem generates cyclic fold bifurcation phenomenon [1] at the maximum reached frequency.

As mentioned, the shooting technique can capture all the periodic motions. Figure 8 depicts the appearance of three periodic solutions (for digital case-000) with different amplitude levels consisting of the upper branch (resonance stable branch, blue), the lower branch (non-resonance stable branch, magenta), and the intermediate branch (unstable branch, orange), which mainly depend on the initial conditions. As the frequency of excitation is increased or decreased, there are jumps in the response amplitude. For the forward excitation frequency sweep, we note that one Floquet multiplier approaches unity at the maximum amplitude of 3.59 $\mu$m, and also the upper stable branch and unstable branch are intersected at the point of the reached maximum frequency. This indicates a cyclic fold bifurcation [1].

Figure 9 compares the dynamic response between theory and experiment at $-12$ dBm AC input signal power [30]. We notice that decreasing the AC source can lower the amplitude response. The frequency response curves experimentally and analytically show the same nonlinear hardening behavior. Thus, we observe a satisfactory agreement for the response among experimental and analytical results.

Next, we notice that electrode D3 (with the smallest air gap), and $V_{\text{Beam}}$ both play a significant role in the operation of the DAC. To clarify the influence of the electrode D3, we select the representative samples digital case-011 (represent the first four cases, D3 'off') and case-111 (represent the last four cases, D3 'on') in figures 10(a) and (b), respectively. From the simulated results, one can notice that lowering $V_{\text{Beam}}$ can make the frequency-swept curve right-shifted and clearly distinguished due to the nonlinear softening effects. Also we note that $V_{\text{Beam}}$ also can generate a big difference for case-011, compared to the case-111.

## 6. Conclusions

In this work, we analytically and experimentally presented modeling, investigation, validation, and optimization of the MEMS resonator-based 3-bit DAC consisting of an in-plane clamped-clamped beam actuated by partial electrodes with different air-gap. First, we derived a dynamic equation of the proposed 3-bit DAC device, and the static response, linear EVPs, and dynamic response were solved then based on the method of the Galerkin-shooting technique. Second, to ensure the DAC function well in the linear domain, we optimized the size of air gaps. The optimized results indicate that the frequency responses ranging from the digital case '000' to '111' are monotonically increasing, linearly ordered, and significantly separated for the output at a single frequency. Third, we experimentally and analytically explored

two samples of the DAC device under the nonlinear operation at −2 dBm and −12 dBm AC power levels, respectively. Forward and backward frequency sweeps were also investigated for all digital cases and were validated with measured results. The frequency response exhibit the characteristic bending toward higher frequencies and show the nonlinear hardening behaviors due to the high mid-plane stretching term. Moreover, we also notice that decreasing the AC power level from −2 dBm to −12 dBm can reduce the amplitude response and swept-range of the frequency curves. Last, we explored and discussed the effects of $V_{\text{Beam}}$ on the DAC operation. Thus, the results suggest that the proposed modeling, simulations, and optimization analysis could be successfully implemented in the design of the DAC under various digital combinations. The rich nonlinear behavior with lower energy consumption could provide some high potential applications in IoT, such as logic, computation, sensing, and actuation.

## Data availability statement

The data that support the findings of this study are available upon reasonable request from the authors.

## Acknowledgment

We acknowledge the financial support from King Abdullah University of Science and Technology (KAUST).

## Appendix

The direct integration of equation (16) can make the simulation very slow when we analyze the dynamic system [40]. To overcome this and improve the efficiency, first, we numerically integrate the complicated terms $F_i(Y)$ and then store the values in a table choosing the step $\Delta Y = 0.05$. Here, the numerical evaluation $F_i(Y)$ is reported.

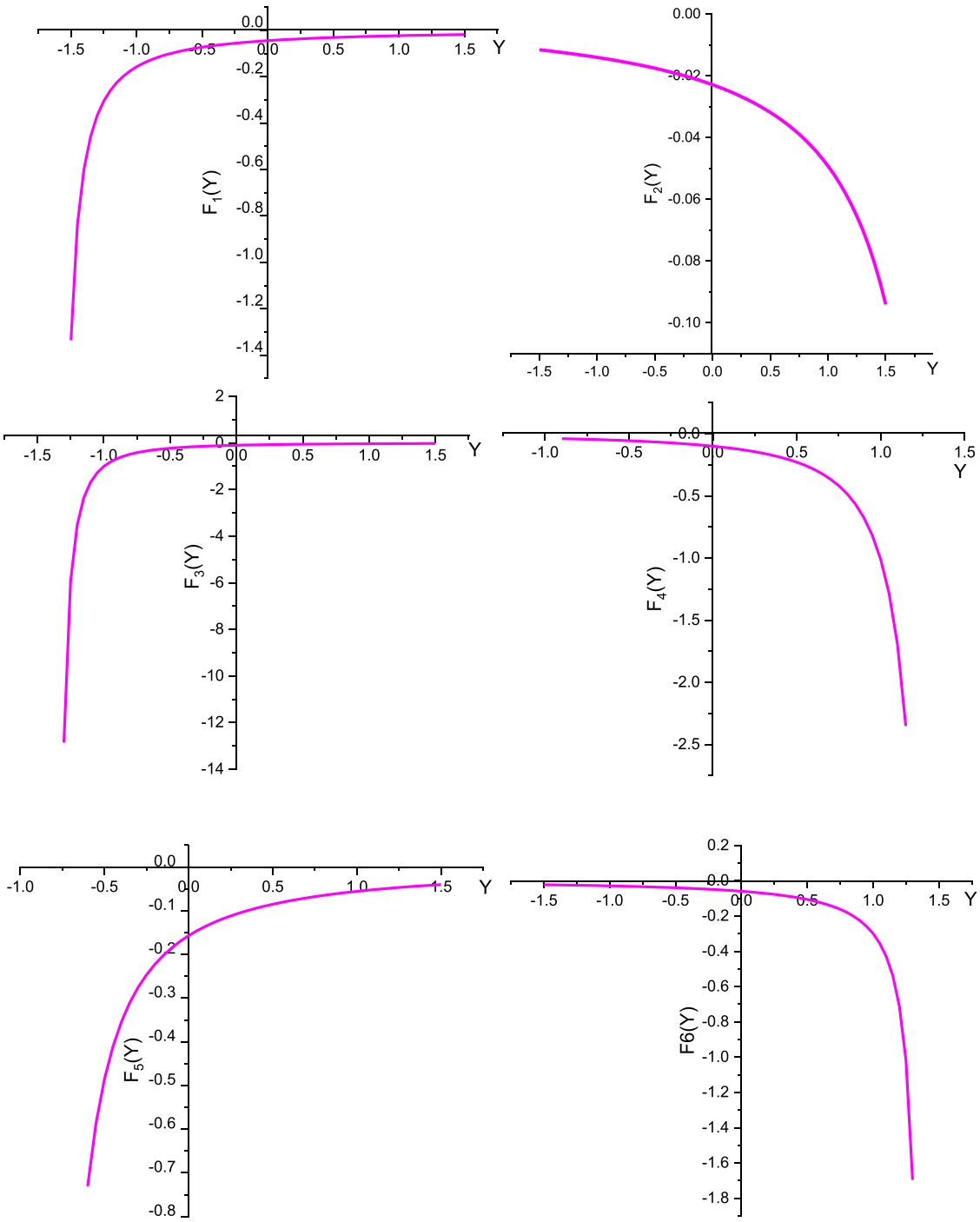


**Figure A.** Evaluations of $F_i(Y)$ by the numerical integration.

## ORCID iD

Wen Zhao https://orcid.org/0000-0001-8159-8195

## References

[1] Younis M I 2011 *MEMS Linear and Nonlinear Statics and Dynamics* (Berlin: Springer)
[2] Nayfeh A and Balachandran B 1995 *Applied Nonlinear Dynamics* (New York: Wiley)
[3] Pacheco S P, Katehi L P B and Nguyen C T-C 2000 Design of low actuation voltage RF MEMS switch *IEEE MTT-S Digest* p 165
[4] Pourkamali S and Ayazi F 2005 Electrically coupled MEMS band pass filters: part II. Without coupling element *Sens. Actuators* A **122** 317–25
[5] Hajhashemi M S, Amini A and Bahreyni B 2012 A micromechanical band pass filter with adjustable bandwidth and bidirectional control of centre frequency *Sens. Actuators* A **187** 10–15
[6] Jeon J, Pott V, Kam H, Nathanael R, Alon E and Liu T-J 2010 Seesaw relay logic and memory circuits *J. Microelectromech. Syst.* **19** 1012–4

[7] Tsai C Y and Chen T L 2010 Design, fabrication, and calibration of a novel MEMS logic gate *J. Microelectromech. Syst.* **20** 095021

[8] Samaali H, Najar F and Chaalane A 2020 Modeling and design of an ultra low-power NEMS relays: application to logic gate inverters *Analog Integr. Circuits Signal Process.* **104** 14–26

[9] Sinha N, Guo Z, Tazzoli A, DeHon A and Piazza G 2012 1 volt digital logic circuits realized by stress-resilient ALN parallel dual-beam MEMS relay *2012 IEEE 25th Int. Conf. Micro Electro Mechanical Systems (MEMS)* pp 668–71

[10] Sinha N, Jones T S, Guo Z and Piazza G 2012 Body-biased complementary logic implemented using ALN piezoelectric MEMS switches *J. Microelectromech. Syst.* **21** 484–96

[11] Ilyas S, Arevalo A, Bayes E, Foulds I G and Younis M I 2015 Torsion based universal MEMS logic device *Sens. Actuators* A **236** 150–8

[12] Noh H, Shim S B, Jung M, Khim Z G and Kim J 2010 Mechanical memory with a DC modulation of nonlinear resonance *Appl. Phys. Lett.* **97** 033116

[13] Yao A and Hikihara T 2013 Counter operation in nonlinear micro-electro-mechanical resonators *Phys. Lett.* A **377** 2551–5

[14] Hajjaj A Z, Jaber N, Ilyas S, Alfosail F K and Younis M I 2020 Linear and nonlinear dynamics of micro and nano-resonators: review of recent advances *Int. J. Non. Linear Mech.* **119** 103328

[15] Mestrom R M C, Fey R H B, Phan K L and Nijmeijer H 2010 Simulations and experiments of hardening and softening resonances in a clamped-clamped beam MEMS resonator *Sens. Actuators* A **162** 225–34

[16] Mestrom R M C, Fey R H B, Van Beek J T M, Phan K L and Nijmeijer H 2008 Modelling the dynamics of a MEMS resonator: simulation and experiments *Sens. Actuators* A **142** 306–15

[17] Venstra W J, Eestra H J R, Gavan K B and Van Der Zant H S J 2009 Magnetomotive drive and detection of clamped-clamped mechanical resonators in water *Appl. Phys. Lett.* **95** 263103

[18] Azizi S, Ghazavi M R, Khadem S E and Cetinkaya G R C 2013 Application of piezoelectric actuation to regularize the chaotic response of an electrostatically actuated micro-beam *Nonlinear Dyn.* **73** 853–67

[19] Hu Y J, Yang J and Kitipornchai S 2013 Snap-through and pull-in analysis of an electro-dynamically actuated curved micro-beam using a nonlinear beam model *J. Sound Vib.* **332** 3821–32

[20] Kumar P, Inamdar M M and Pawmark D N 2020 Characterization of the internal resonances of a clamped-clamped beam MEMS resonator *Microsyst. Technol.* **26** 1–17

[21] Ghayesh M H, Farokhi H and Amabili M 2013 Nonlinear behavior of electrically actuated MEMS resonators *Int. J. Eng. Sci.* **71** 137–55

[22] Li L, Wang Q and Han J 2017 Nonlinear coupled vibration of electrostatically actuated clamped-clamped microbeams under higher-order modes excitation *Nonlinear Dyn.* **90** 1593–606

[23] Choi B and Lovell E G 1997 Improved analysis of micro beams under mechanical and electrostatic loads *J. Micromech. Microeng.* **7** 24

[24] Nayfeh A, Younis M I and Abdel-Rahman E M 2007 Dynamic pull-in phenomenon in MEMS resonators *Nonlinear Dyn.* **48** 153–63

[25] Younis M I, Abdel-Rahman E M and Nayfeh A 2003 A reduced-order model for electrically actuated microbeam-based MEMS *J. Microelectromech. Syst.* **12** 672–80

[26] Yu Y, Wu B and Lim C W 2012 Numerical and analytical approximations to large post-bucking deformation of MEMS *Int. J. Mech. Sci.* **55** 95–103

[27] Emam S A and Nayfeh A H 2004 Nonlinear response of buckled beams to subharmonic-response excitations *Nonlinear Dyn.* **35** 105–22

[28] Nayfeh A and Younis M I 2005 Dynamics of MEMS resonators under superharmonic and subharmonic excitation *J. Micromech. Microeng.* **15** 1840–7

[29] Zhou G, Tay F E, Chau F S, Zhao Y and Logeeswaran V J 2004 Micromechanical torsional digital-to-analog converter for open-loop angular positioning applications *J. Micromech. Microeng.* **14** 737

[30] Yeh R, Conant R A and Pister K S 1999 Mechanical digital to analog converters *Tenth Int. Solid-State Sensors and Actuators Conf.* pp 998–1001

[31] Toshiyoshi H, Kobayashi D, Mita M, Hashiguchi G, Fujita H, Endo J and Wada Y 2000 Microelectromechanical digital-to-analog converter of displacement for step motion actuators *J. Microelectromech. Syst.* **9** 218–25

[32] Pandiyan P, Uma G and Umapathy M 2017 Design and simulation of MEMS- based digital-to-analog converters for in-plane actuation *Arab J. Sci. Eng.* **42** 4991–5001

[33] Ahmed S, Zou X C and Fariborzi H 2019 Micro-resonator based digital to analog converter for ultralow power applications *2019 20th Int. Conf. Solid-State Sensors, Actuators and Microsystems & Eurosensors XXXIII (TRANSDUCERS & EUROSENSORS XXXIII)* (IEEE) pp 821–4

[34] Ahmed S, Zou X C, Jaber N, Mohammad M I and Fariborzi H 2020 A low power micro electromechanical resonator based digital to analog converter *J. Microelectromech. Syst.* **29** 320–8

[35] Cowen G H A, Monk D, Wilcenski S, Hardy B and Inc M *SOLMUMPs Design Handbook* (available at: www.memscap.com/products/mumps/soimumps/referencematerial) (Accessed June 2018)

[36] Younis M I and Nayfeh A 2003 A study of the nonlinear response of a resonant microbeam to an electric actuation *Nonlinear Dyn.* **31** 91–117

[37] Abdel-Rahman E M, Younis M I and Nayfeh A 2002 Characterization of the mechanical behavior of an electrically actuated microbeam *J. Micromech. Microeng.* **12** 759

[38] Powell M J 1978 A fast algorithm for nonlinear constrained optimization calculations *Numerical Analysis* (Berlin: Springer)

[39] Ruzziconi L, Younis M I and Lenci S 2013 An efficient reduced-order model to investigate the behavior of an imperfect microbeam under axial load and electric excitation *J. Comput. Nonlinear Dyn.* **8**

[40] Ruzziconi L, Bataineh A M, Younis M I, Cui W and Lenci S 2013 Nonlinear dynamics of an electrically actuated imperfect microbeam resonator: experimental investigation and reduced-order modeling *J. Micromech. Microeng.* **23** 075012